Supporting Information

Ternary-Dielectric Dual-Domain Triboelectric Nanogenerator for High Charge Density and Tail-Charge Suppression

Sihang Gao, ‡*[a] Yuqi Sun, ‡[a] Lingjiang Long,[a] Yongqi Liu,[a] Jiyu Wang*[b]

‡ S. Gao and Y. Sun contributed equally to this work

[a] School of Automation, Chongqing University of Posts and Telecommunications, Chongqing, 400065, China

[b] State Key Laboratory of Advanced Electromagnetic Technology, Huazhong University of Science and Technology, Wuhan 430074, China

E-mail: gaosh@cqupt.edu.cn; jiyuwang@hust.edu.cn

Content of the Supplementary information

Video S5 Demonstration of the wind-water co-rotary TDT working for wind and water energy collection.

Table S1 Comparison with the reported high-performance sliding TENGs.

Table S2 Comparison of the mechanical-to-electrical energy conversion efficiency of this work with other structures.

Table S3 Energy distribution in the rotary TDT system from mechanical input to electrical output.

Note S1 Detailed theoretical derivation of the quasi static capacitive model of the sliding TENG

Note S2 Detailed calculation of the mechanical-to-electrical energy conversion efficiency of the TDT

Note S3 Detailed calculations of the energy efficiency of the PMC

Note S4 Energy flow analysis and net energy balance of the system

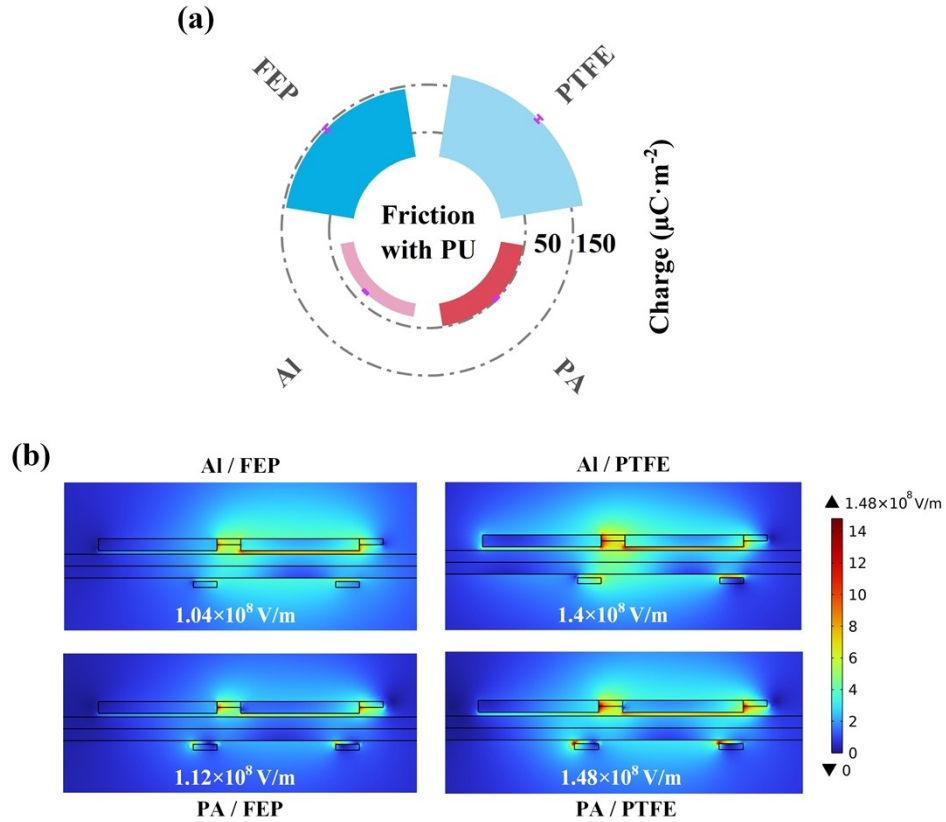

Fig. S1 The comparison of the charge transfer performance of various common friction materials paired with PU foam, including a) Quantitative results and b) COMSOL simulation results.

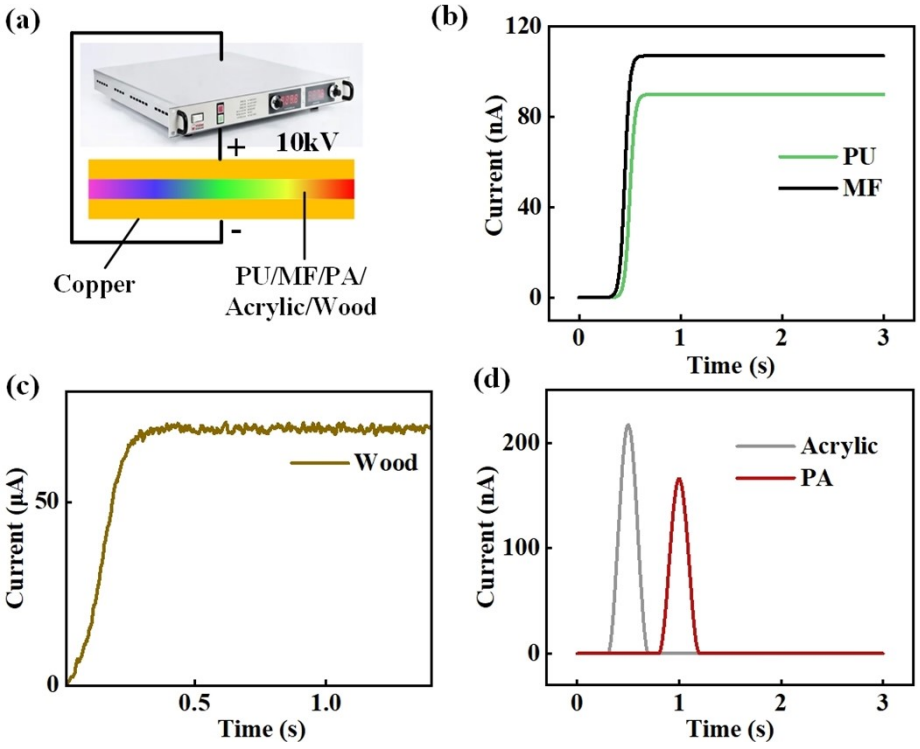

Fig. S2 Comparison of current responses of different materials under high voltage DC electric field, including a) High voltage DC testing system, b) Current responses of porous dielectrics, c) Current responses of wood, d) Current responses of dense dielectrics.

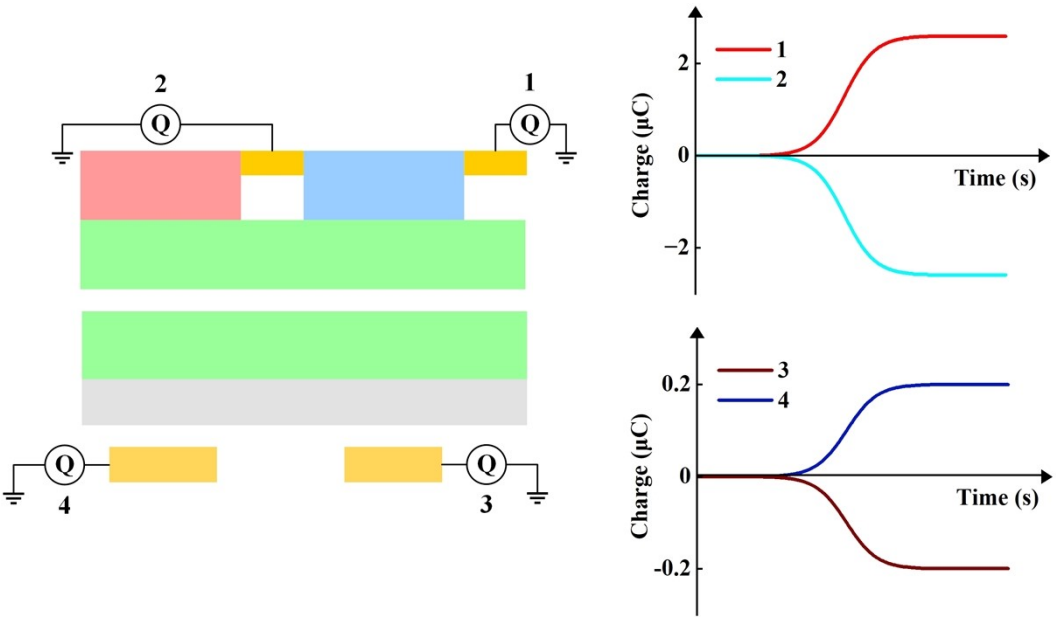

Fig. S3 Charge collection characteristics of each TDT electrode.

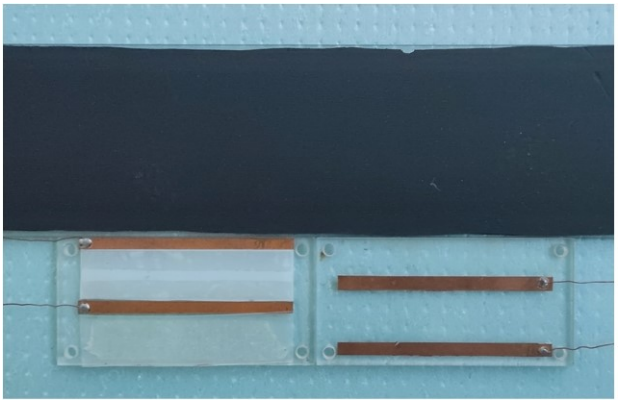

Fig. S4 The physical picture of TDT slider.

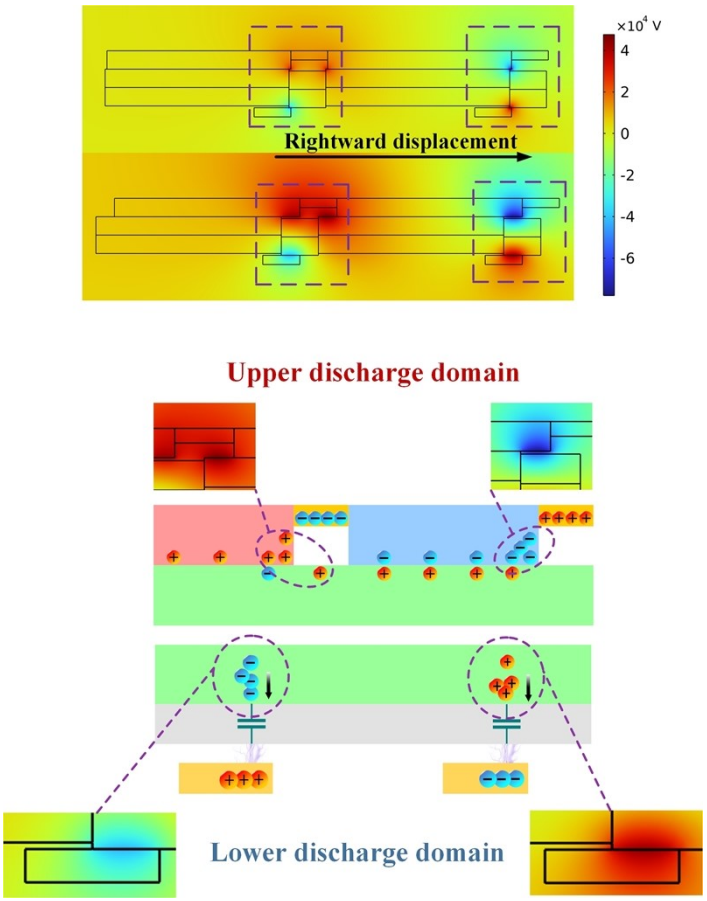

Fig. S5 COMSOL simulation of the potential distribution during the TDT sliding process.

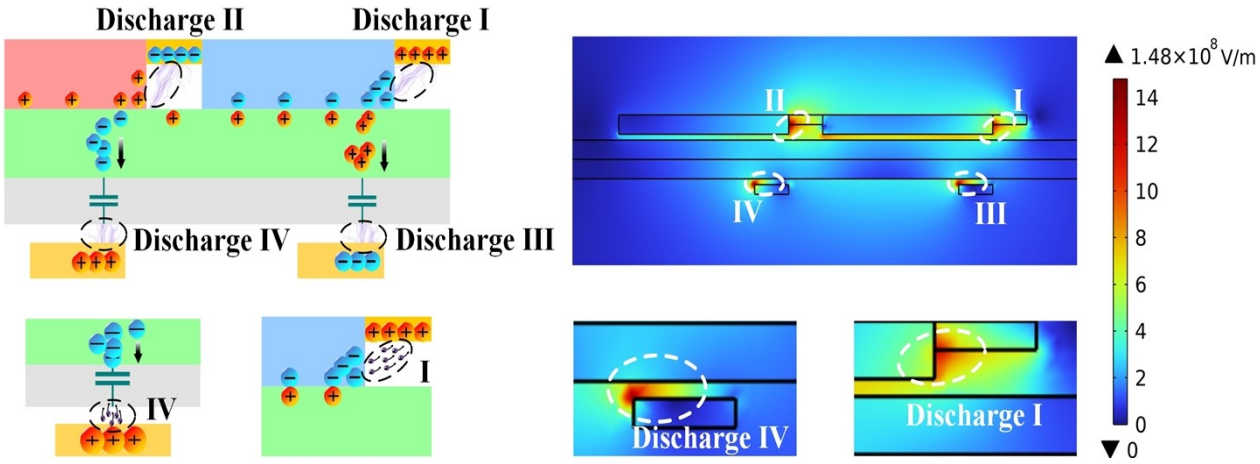

Fig. S6 COMSOL simulation of the electric field strength distribution after TDT sliding.

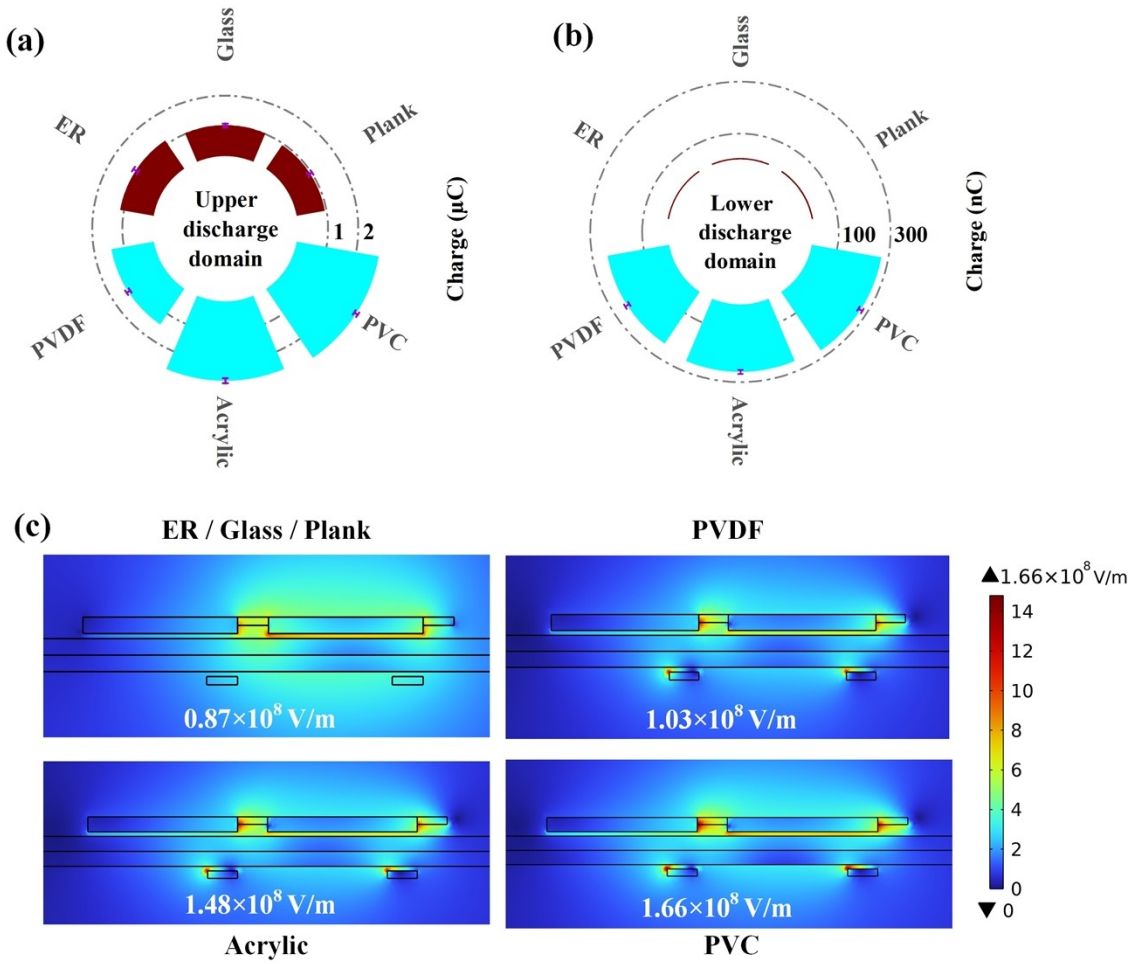

Fig. S7 The comparison of the charge transfer performance of various substrate materials materials, including a) Quantitative results of the upper discharge region, b) Quantitative results of the lower discharge region, c) COMSOL simulation results.

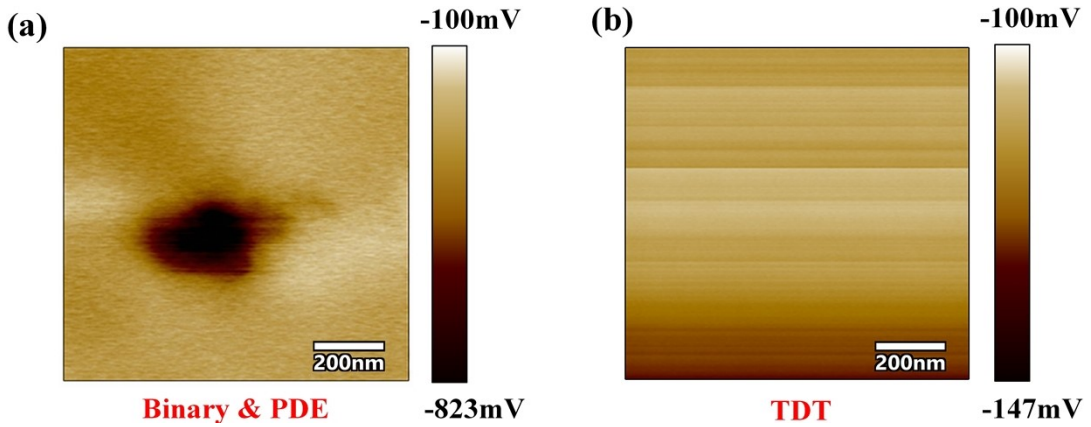

Fig. S8 KPFM characterization diagram for demonstrating the effective removal of tail charges, including a) Binary structure, b) TDT structure.

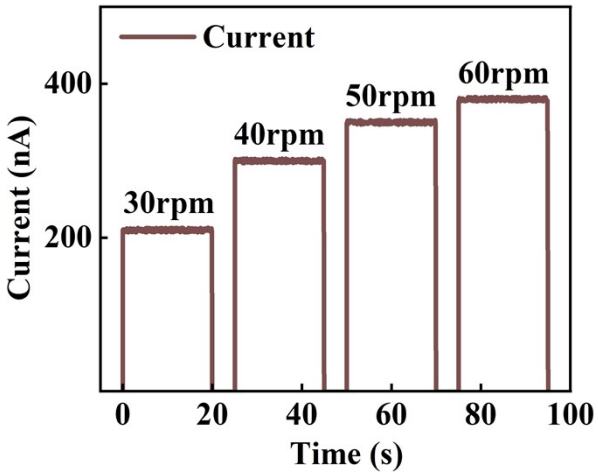

Fig. S9 The I_{sc} of the upper discharge domain in TDT on varied sliding speeds.

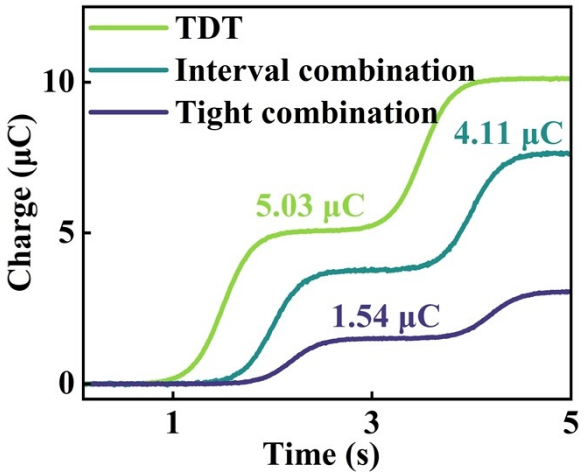

Fig. S10 The Q_{sc} of the TDT and binary structures under the same contact area.

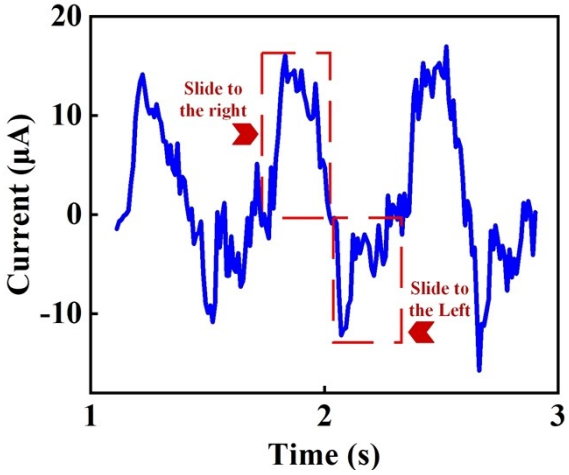

Fig. S11 The I_{sc} of the upper discharge domain in TDT during the reciprocating sliding.

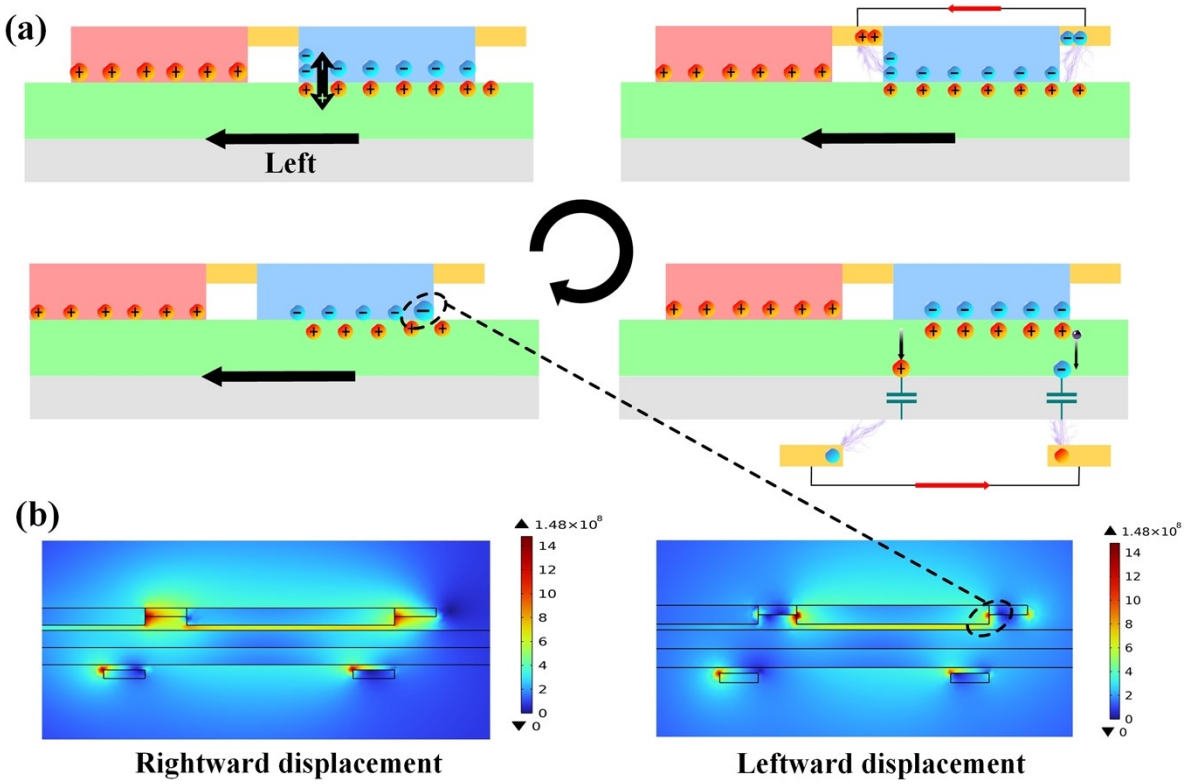

Fig. S12 The working principle of the TDT during the reverse sliding, including a) Schematic of the working principle and b) COMSOL simulation results.

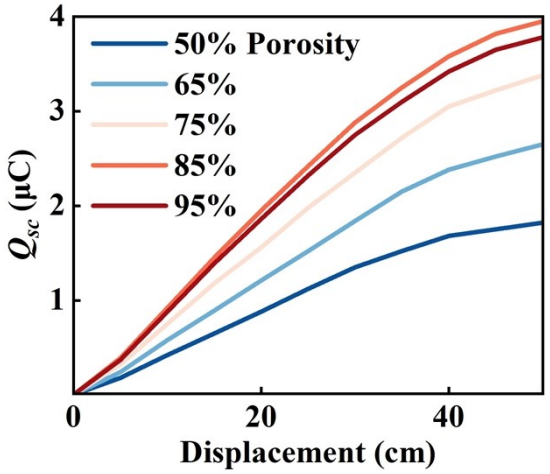

Fig. S13 The sensitivity of TDT's Q_{sc} to the porosity of PU foam.

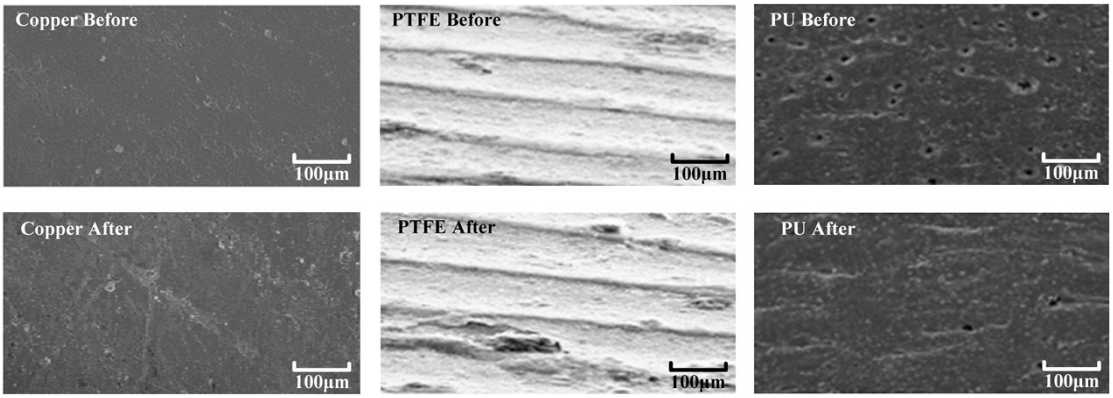

Fig. S14 SEM microscopic morphology images of the electrode and dielectric layers after long-term operation.

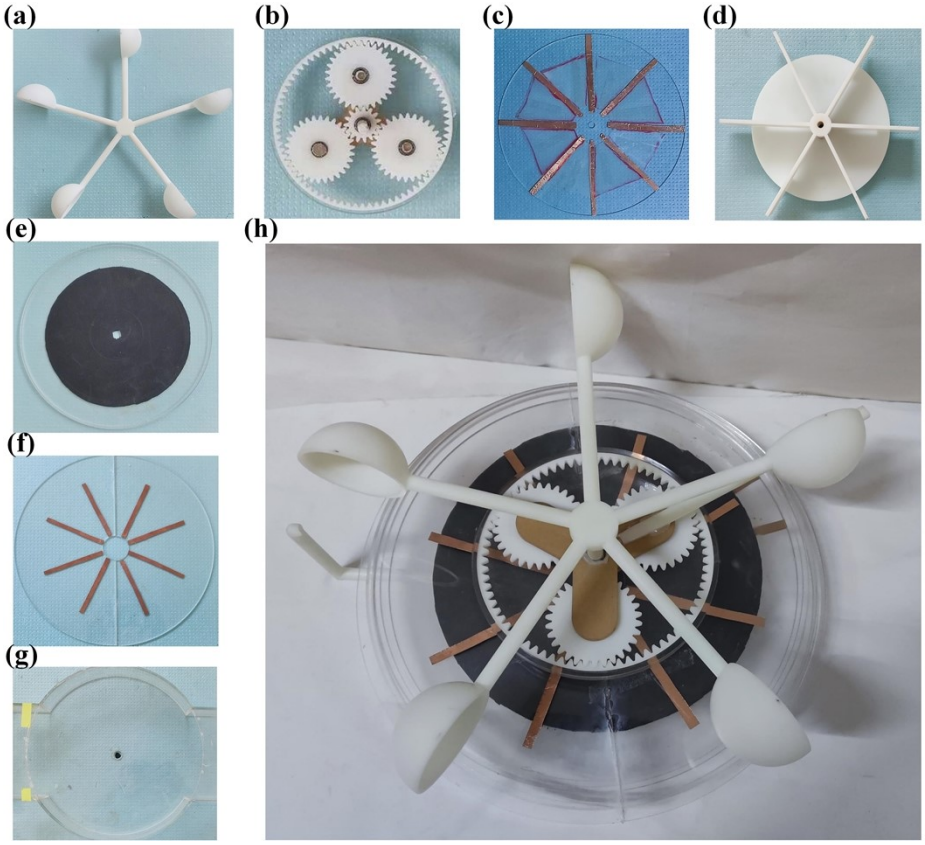

Fig. S15 The overall and component pictures of the high-output rotary TDT, including a) Wind cups, b) Counter-rotating gear, c) Central layer, d) Water wheel, e) PU layer, f) PDE layer, g) Diversion trench, h) Rotary TDT.

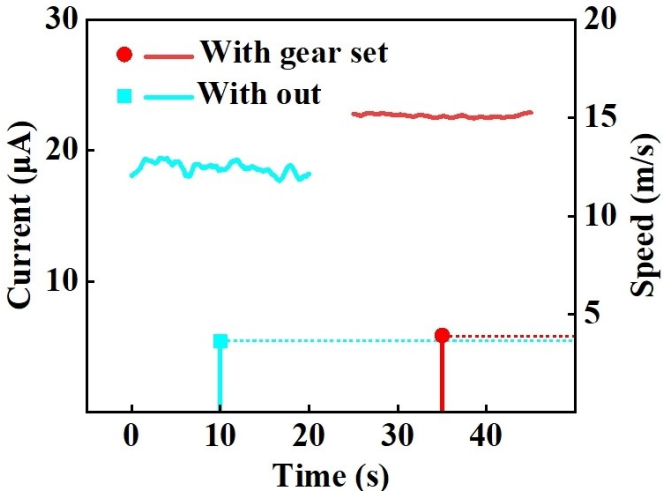

Fig. S16 The comparison of the I_{sc} and cut-in wind speed of the high-output rotary TDT with and without the gear.

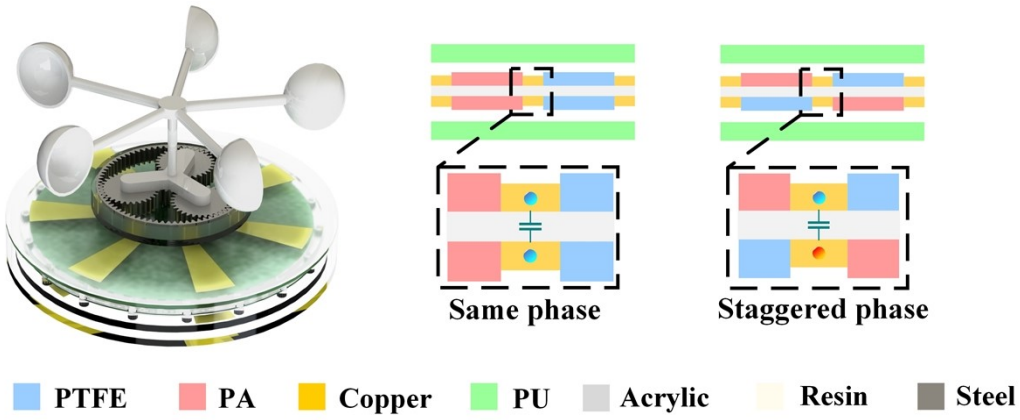

Fig. S17 Schematic of the dual-layer triboelectric generation based on the symmetrical TDT structure.

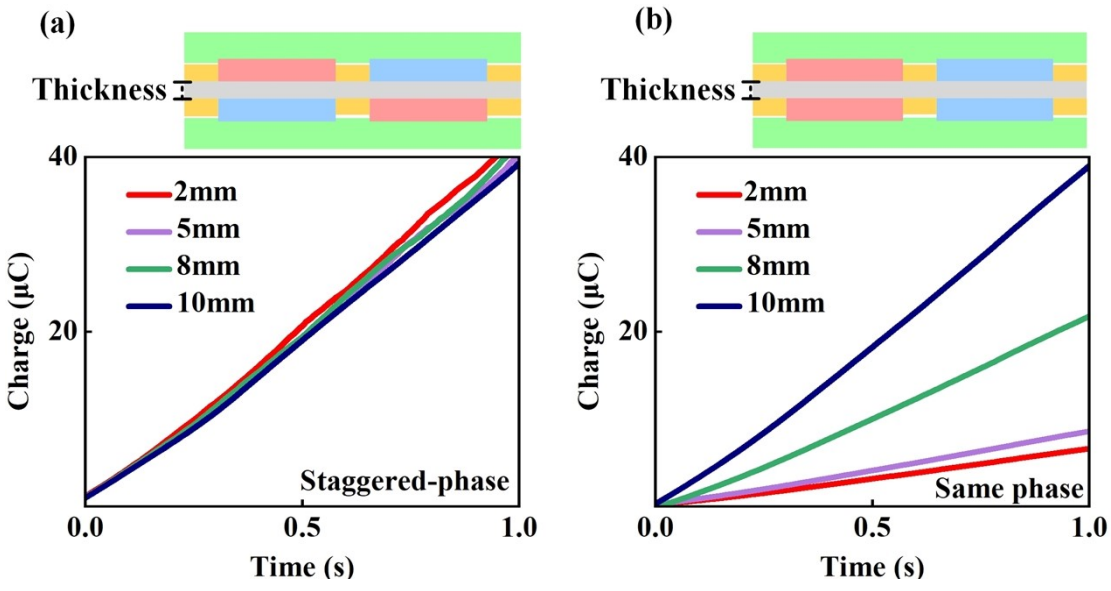

Fig. S18 The Q_{sc} of the the high-output rotary TDT with different thickness of the acrylic substrate, including a) Staggered-phase structure and b) Same-phase structure.

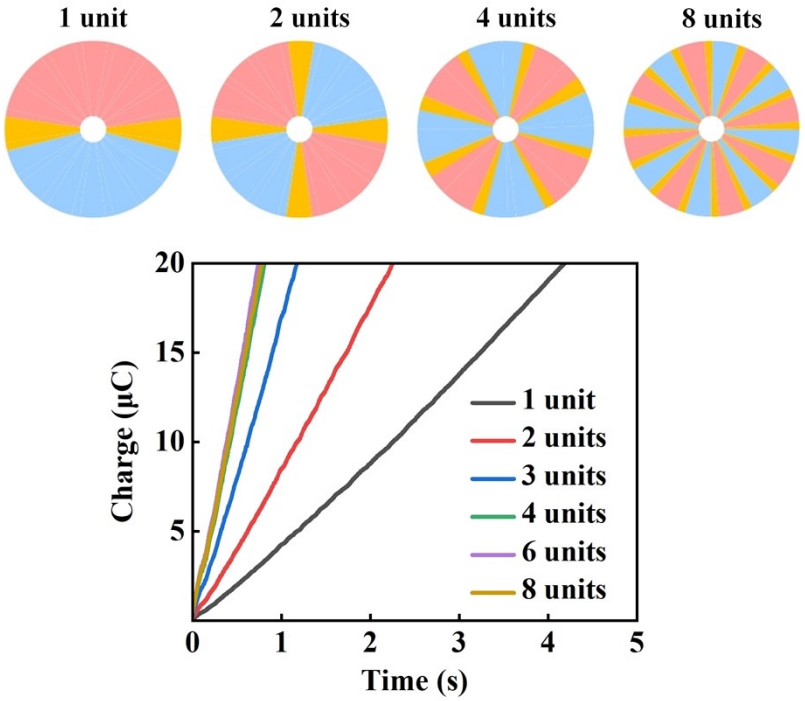

Fig. S19 The Q_{sc} of the high-output rotary TDT with different number of the TDT units.

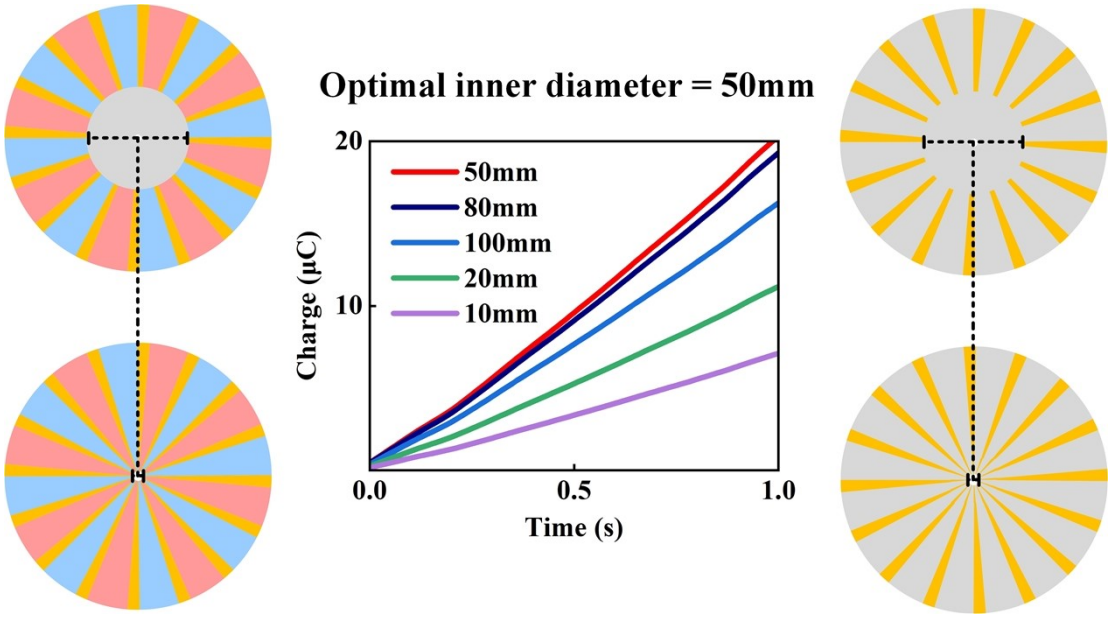

Fig. S20 The Q_{sc} of the high-output rotary TDT with different inner diameters of the coated materials.

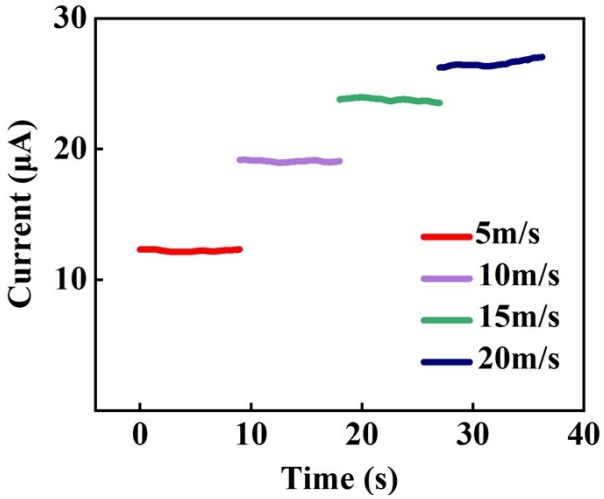

Fig. S21 The I_{sc} of the high-output rotary TDT under different wind speeds.

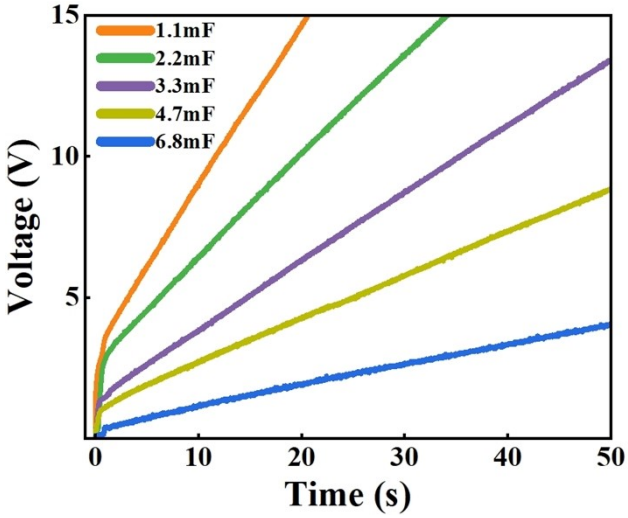

Fig. S22 The charging rates of the capacitors with different capacitances by the high-output rotary TDT.

Fig. S23 Application of the water-wheel-driven rotary TDT.

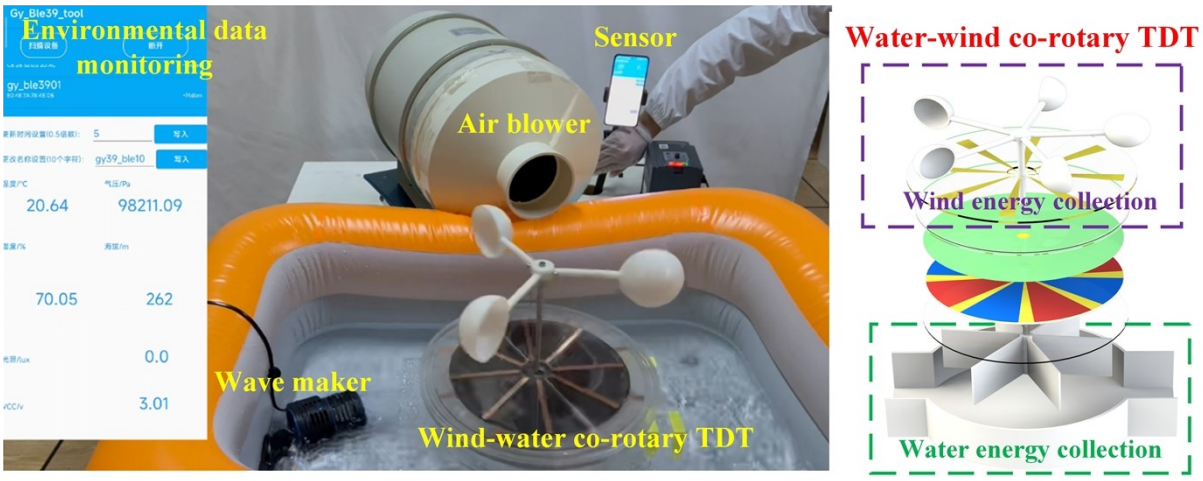

Fig. S24 Application of the wind-water co-rotary TDT.

Table S1. Comparison with the reported high-performance sliding TENGs.

Article	Output Power	Output Energy	Effective area	Output power density	Output energy density
Li et al. *Adv. Mater.* (2025)[1]	82.22 mW	24.17 mJ	48 cm^2	17.13 Wm^{-2}	5035 mJ m^{-2}
Shan et al. *Adv. Funct. Mater.* (2023)[2]	33.64 mW	/	27 cm^2	12.4 Wm^{-2}	/
Li et al. *Energy Environ. Sci.* (2024)[3]	7.91 mW	3.85 mJ	36 cm^2	2.2 Wm^{-2}	1069 mJ m^{-2}
Fu et al. *Adv. Mater.* (2023)[4]	40.9 mW	2.38 mJ	19.8 cm^2	20.7 Wm^{-2}	1200 mJ m^{-2}
He et al. *Adv. Mater.* (2022)[5]	116.9 mW	1.35 mJ	60 cm^2	19.48 Wm^{-2}	225 mJ m^{-2}
Gao et al. *Nano energy* (2024)[6]	8.3 mW	/	13 cm^2	6.4 Wm^{-2}	/
This work	54.07 mW	8.2 mJ	24 cm^2	22.53 Wm^{-2}	3417 mJ m^{-2}

References

1. K. Li, S. Gong, X. Wang, S. Fu, H. Wu, J. Wang, S. Xu, G. Li, C. Shan, C. Hu, *Adv. Mater*., 2025, **37**, 2418478.
2. C. Shan, K. Li, H. Wu, S. Fu, A. Liu, J. Wang, X. Zhang, B. Liu, X. Wang, C. Hu, *Adv. Funct. Mater*., 2024, **34**, 2310332.
3. K. Li, S. Gong, S. Fu, H. Guo, C. Shan, H. Wu, J. Wang, S. Xu, G. Li, Q. Zhao, X. Wang and C. Hu, *Energy Environ. Sci*., 2024, **17**, 8942.
4. S. Fu, H. Wu, W. He, Q. Li, C. Shan, J. Wang, Y. Du, S. Du, Z. Huang, C. Hu, *Adv. Mater*., 2023, **35**, 2302954.
5. W. He, C. Shan, S. Fu, H. Wu, J. Wang, Q. Mu, G. Li, C. Hu, *Adv. Mater*., 2023, **35**, 2209657.
6. S. Gao, H. Wei, R. Wang, X. Luo, Y. Liu, C. Huang, Y. Lei, X. Deng, *Nano Energy*, 2024, **129**, 110060.

Table S2. Comparison of the mechanical-to-electrical energy conversion efficiency of this work with other structures.

Reference	Operation mode	M-E Efficiency
Adv. Energy Mater. 2022, 2202627	Sliding	21.9%
Adv. Mater. 2022, 2202238	Solid-liquid	24.89%
Adv. Funct. Mater. 2021, 2105237	Contact-separation	29.7%
Nano Energy 2024, 110060	Binary-dielectric architecture	16.7%
This work for comparison	Ternary-dielectric architecture	27.35%
This work for comparison	Binary-dielectric dual-domain architecture	23.4%
This work	Ternary-dielectric dual-domain architecture	**33.8%**

References

1. B. Cao, P. Wang, P. Rui, X. Wei, Z. Wang, Y. Yang, X. Tu, C. Chen, Z. Wang, Z. Yang, T. Jiang, J. Cheng, Z. L. Wang, Adv.EnergyMater., 2022, 12, 2202627.
2. Y. Zheng, T. Liu, J. Wu, T. Xu, X. Wang, X. Han, H. Cui, X. Xu, C. Pan, X. Li, Adv.Mater., 2022, 34, 2202238.
3. Z. Lin, B. Zhang, Y. Xie, Z. Wu, J. Yang, Z. L. Wang, Adv.Funct.Mater., 2021, 31, 2105237.
4. S. Gao, H. Wei, R. Wang, X. Luo, Y. Liu, C. Huang, Y. Lei, X. Deng, NanoEnergy, 2024, 129, 110060.
5. C. Shan, K. Li, H. Wu, S. Fu, A. Liu, J. Wang, X. Zhang, B. Liu, X. Wang, C. Hu, *Adv. Funct. Mater.,* 2024, **34**, 2310332.
6. K. Li, S. Gong, S. Fu, H. Guo, C. Shan, H. Wu, J. Wang, S. Xu, G. Li, Q. Zhao, X. Wang and C. Hu, *Energy Environ. Sci.*, 2024, **17**, 8942-8953.

Note S1. Detailed theoretical derivation of the quasi static capacitive model of the sliding TENG

According to the quasi-static capacitive model of a TENG, the short-circuit transferred charge Q_{sc} represents the induced charge that must flow between the electrodes to maintain zero potential difference between them. For a sliding-mode TENG, Q_{sc} as a function of displacement x can be expressed by (1).

$$Q_{sc}(x) = C(x) \cdot V_{oc}(x) \tag{1}$$

where $V_{oc}(x)$ is the open-circuit voltage arising from the triboelectric charges when the external circuit is open, as expressed by (2). $C(x)$ is the position-dependent capacitance between the electrodes.

$$V_{oc}(x) = \frac{\sigma \cdot d}{\varepsilon_0} \tag{2}$$

where σ is the surface charge density, d is the effective dielectric thickness, and ε_0 is the vacuum permittivity.

The capacitance $C(x)$ is essentially that of a parallel-plate capacitor determined by the overlapping area $S(x)$, as expressed by (3).

$$C(x) = \frac{\varepsilon_0 \cdot S(x)}{d} \tag{3}$$

Combining these expressions leads to (4). Thus, the transferred charge Q_{sc} is primarily governed by the surface charge density σ and the effective contact area $S(x)$, both of which are independent of sliding speed under the conditions of full contact and charge saturation.

$$Q_{sc}(x) = \sigma \cdot \Delta S(x) \tag{4}$$

Note S2. Detailed calculation of the mechanical-to-electrical energy conversion efficiency of the TDT

A micro force sensor was integrated into the linear sliding platform to accurately quantify the input mechanical work of the TDT during the sliding. The sensor records the friction force during sliding in real time, and the input mechanical work is calculated by integrating the force over the sliding displacement. Simultaneously, the electrical output is measured under the optimal matched load to determine the converted electrical energy per cycle.

The input mechanical work (W_{mech}) of the TDT within a single sliding cycle can be expressed by (1).

$$W_{mech} = \int_0^s F(x)dx \tag{1}$$

where $F(x)$ is the friction force and s is the sliding displacement.

The output electrical energy (E_{elec}) of the TDT within a single sliding cycle can be expressed by (2).

$$E_{elec} = \int_0^t \frac{V^2(t)}{R} dt \tag{2}$$

where $V(t)$ is the real-time output voltage across the matched load R.

Thus, M-E conversion efficiency (η_{M-E}) can be expressed by (3).

$$\eta_{M-E} = \frac{E_{elec}}{W_{mech}} \times 100\% \tag{3}$$

Note S3. Detailed calculations of the energy efficiency of the PMC

The energy conversion efficiency η_{PMC} is defined as the ratio of the energy delivered to the load (E_{out}) to the energy released from the buffer capacitor (E_{in}) within one complete triggering cycle. facilitate reliable triggering of the thyristor, a relatively small buffer capacitor C_1 was selected, enabling the Zener diode to break down rapidly and initiate the discharge process. Considering that the front-stage capacitor still retains a residual voltage V_{low} after discharging. The input energy E_{in} is determined by the voltage change across the buffer capacitor C_1 at the triggering moment as expressed by (1).

$$E_{in} = \frac{1}{2} C_1 (V_{up}^2 - V_{low}^2) \tag{1}$$

where C_1 is the buffer capacitance, V_{up} is the trigger-on voltage, and V_{low} is the residual voltage after discharge.

The output energy E_{out} stored in the output capacitor C_{load} is given by (2).

$$E_{out} = \frac{1}{2} C_{load} V_{end}^2 \tag{2}$$

where C_{load} is the load capacitance and V_{end} is the voltage after charging (1.3V).

Thus, the conversion efficiency η_{PMC} for a single cycle is calculated as follows.

$$\eta_{PMC} = \frac{E_{out}}{E_{in}} \times 100\% \tag{3}$$

Substituting the measured values (C_1=4.7 μF, V_{up}=8.0 V, V_{low}=2.1 V C_{load}=150 μF, V_{end}=1.3 V) yields $\eta_{PMC} \approx 90.5\%$ for a representative cycle. On the whole, the average efficiency of 87.2% is obtained from multiple measurements on varied load conditions.

Note S4. Energy flow analysis and net energy balance of the system

(1) Net energy balance model

The overall energy balance of the system follows the law of energy conservation, as expressed by (1).

$$W_{mech} = E_{available} + Q_{friction} + E_{loss(PMC)} \quad (1)$$

where W_{mech} is the total external mechanical work input, and $E_{available}$ is the net energy stored in the load capacitor and available for use by electronic devices.

(2) Quantitative energy flow analysis

Based on experimentally measured efficiency metrics, the energy conversion pathway of the rotary TDT system can be divided into two key stages.

①Mechanical-to-electrical energy conversion efficiency

The measured electromechanical conversion efficiency of the TDT module (η_{M-E}) is 33.8%, the detailed calculation of the mechanical to electrical conversion efficiency can be seen in **Note S2(ESI†)**. Approximately 66.2% of the mechanical energy is dissipated as vibration losses, ionization internal losses, or frictional heat ($Q_{friction}$). This efficiency level is notably higher than that of conventional binary structures.

②PMC efficiency

The conversion efficiency of the power management circuit (η_{PMC}) under matched load conditions is approximately 87.2%, as depicted in **Note S3 (ESI†).**

③Net output efficiency of the system

The final net output efficiency of the system can be calculated by (2). Approximately 4.3% of the total energy is dissipated as heat during LC resonant matching and SCR triggering ($E_{loss(PMC)}$). Thus, the rotary TDT system achieves a net energy balance rate of about 29.5%, demonstrating significant competitiveness in the field of environmental mechanical energy harvesting.

$$\eta_{Net} = \eta_{M-E} \times \eta_{PMC} = 33.8\% \times 87.2\% \approx 29.5\% \quad (2)$$

Table S3. Energy distribution in the rotary TDT system from mechanical input to electrical output.

Component	**Proportion (%)**	**Physical destination**
Net available energy ($E_{available}$)	29.5%	Stored in capacitor, used to drive external load circuits
Mechanical frictional loss ($Q_{friction}$)	66.2%	Interfacial frictional heat, mechanical vibration dissipation, ionization losses
Circuit conversion loss ($E_{loss(PMC)}$)	4.3%	LC loop internal resistance heating, diode voltage drop losses
Total (W_{mech})	100%	Total system energy input